
CONTRIBUTED PAPERS

STRUCTURAL CHARACTERIZATION OF THIN FILMS BY X-RAY REFLECTIVITY

ISAO KOJIMA AND BOQUAN LI

Department of Analytical Chemistry, National Institute of Materials and Chemical Research, 7-1 Higashi, Tsukuba, Ibaraki 305-8565

1. Introduction

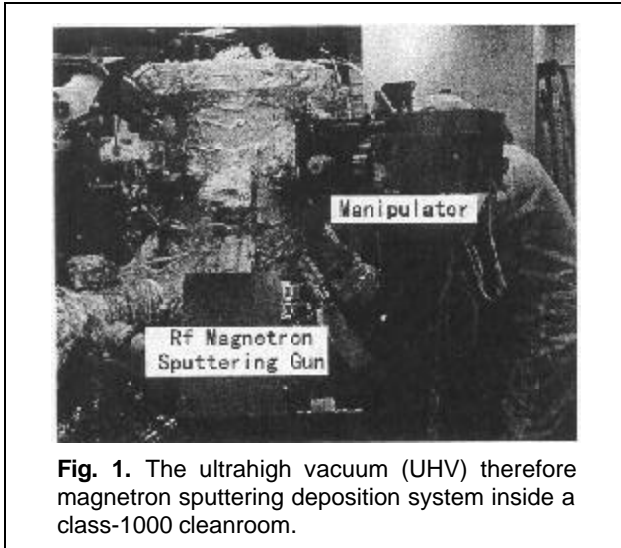
The increased packing density of semiconductor devices drives the dimensions of these devices down. The gate oxide of the new-generation memory cells such as giga-bit dynamic random access memories (DRAMs) is projected to be only a few nanometers [1, 2]. X-ray mirrors [3-5], giant magnetoresistance multilayers [6], magnetic disks, and other functional devices are all composed of ultra-thin films. The physical properties and performance of these devices often crucially depend on their interfacial structures. Therefore, atomic level control and characterization of the structure of the ultra thin films have become increasingly important. Surface analysis techniques are widely used in the characterization of semiconductor thin films, as well as in in-situ monitoring device production processes. With the continuing minimization of thin film devices, characterization techniques with high reliability and precision are required. To this end, it is necessary to develop reference material, such as surface analysis reference material as suggested by ISO/TC201, to calibrate the resolution of these techniques [7]. To meet the demand of the standardization of surface analysis, we have been aimed at developing reference multilayer material [8, 9] for ultra-thin film characterization. X-ray reflectivity (XRR) is believed to be able to offer accurate thickness values for both thin films and multilayers with the same precision, as well as densities, surface and interface roughnesses [10, 11]. We are interested in exploring and checking the accuracy and precision of XRR when used to determine the thickness and density of multilayer reference material [12-14]. In this article, we summarize some of our XRR characterization results of thin films [15-25]. Firstly, the characterization of Pt thin films deposited at various thicknesses and

temperatures is discussed [18, 19]. Noble metal Pt thin films are stable in air. Therefore, there is no oxide on the film surface. The density of the Pt thin films determined by XRR was found to be consistent with that by mass measurement method. The difference is about 1%. The surface roughness of the Pt thin films determined by XRR is in good agreement with that by atomic force microscope (AFM). However, the surface roughness determined by the two methods, according to our experience, is usually different when native oxides are formed on the surfaces. Secondly, we discuss a higher density, nanometer-thick interface layer formed by sputter depositing SiO₂ on Si substrate and determined by XRR [20-22]. This shows XRR is a promising probe for nondestructive and quantitative interface characterization. Finally, the XRR characterization on sputter deposited SiO₂/Si and Si₃N₄/Si multilayers, as well as molecular beam epitaxy (MBE) grown GaAs/AlAs superlattice, is discussed [23-25], which is consistent with transmission electron microscope (TEM) study. All these results demonstrate XRR is able to offer quantitative structural information of thin films and multilayers. Its nondestructive feature makes it a very attractive technique.

2. Experimental Methods

2.1. Film Deposition Systems

Figure 1 shows the picture of our rf magnetron sputtering system which consists of three rf sputtering guns and one rf radical gun. Film deposition was carried out in an ultrahigh vacuum (UHV, base pressure 1×10^{-8} Pa) condition. The sputtering gun was carefully aligned to 35° offset from the substrate normal and 60 mm offset from the substrate center. With this special design, excellent film thickness uniformity, less than 1% deviation in thickness over a



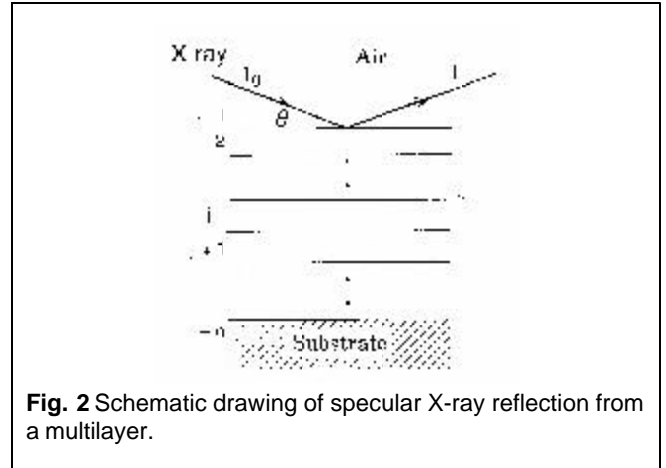
3 inch wafer, can be achieved. The details of the system have been described elsewhere [26]. Connected to the sputtering chamber is a same-sized molecular beam epitaxy (MBE) chamber.

Before deposition, the native oxide on the silicon surface was removed by dipping into diluted HF solution for Si(100) and into 1% buffered HF solution (7: 1 NH₄F: HF) for Si(111) wafers, respectively.

2.2. X-ray Reflectivity Measurement

X-ray reflectivity measurements were performed using a high-resolution X-ray diffractometer (Rigaku SLX-2000). A rotating anode Cu K α source (18kW) was used and the X-ray beam was monochromatized using a channel-cut Ge(220) monochromator. The incident and reflected beams were collimated with slits of 0.05 mm in width and 2 mrh in height and the reflection intensity was measured by a scintillation counter. The specular reflectivity curves were recorded with a ω - 2θ scan.

To determine thickness and roughness with high accuracy, it is essential to precisely align a sample position to the X-ray beam. The sample is mounted on a vertical sample stage, which is installed on a higher resolution goniometer. The 2θ angular resolution of the instrument is 0.0002°. The alignment process is controlled by a computer and carried out automatically. By repeatedly adjusting z and ω (or θ) positions, an optimum position is obtained in which the sample is located at the center of the X-ray beam and only half X-ray beam is detected by the detector. Then, by setting the detector (2θ) at an appropriate position, the total external reflection adjustment starts. By further optimizing the z , ω and χ positions,



maximum reflection intensity which equals the intensity of the incident beam is achieved.

2.3. Principle and Calculation Procedures of X-ray Reflectivity

When an X-ray beam (I_0) impinges with a grazing incidence angle on N layered thin films (shown in Fig. 2), a reflectivity is defined as:

$$|r_{12}|^2 = I/I_0 \quad (1)$$

where, I is the reflected X-ray intensity. The recursion formula is

$$r_{j,j+1} = \frac{r_{j+1,j+2} + F_{j,j+1}}{r_{j+1,j+2} \times F_{j,j+1} + 1} a_j^4 \quad (2)$$

where,

$$F_{j,j+1} = \frac{g_j - g_{j+1}}{g_j + g_{j+1}} \exp\left(-8\pi^2 g_j g_{j+1} \sigma_{j+1}^2 / \lambda^2\right) \quad (3)$$

$$a_j = \exp\left[-i\pi g_j d_j / \lambda\right] \quad (4)$$

where θ is the incidence angle, λ is the wavelength, d_j and a_j are the j^{th} layer thickness and surface roughness. The recursive equation was first obtained by Parratt for the X-ray reflectivity simulation [27]. The roughness term was introduced in the framework of distorted wave Born approximation [28].

There are 4 parameters for each layer, such as δ , β , thickness and roughness. The δ and β parameters are related to the refractive index n of a material

$$N=1-\delta-i\beta, \quad (6)$$

where

$$\delta=(r_e/2\pi)\lambda^2 N_0 \rho \sum X_i(Z_i+f_i')/\sum X_i M_i \quad (7)$$

$$\beta=(r_e/2\pi)\lambda^2 N_0 \rho \sum X_i f_i''/\sum X_i M_i \quad (8)$$

r_e is the classical radius of an electron, N_0 is the Avogadro constant, ρ is the density of the material, Z_i , M_i and X_i are the atomic number, weight and ratio respectively, and f' and f'' are the atomic scattering factors.

The least-square calculation was performed in order to minimize the χ^2 value, which is expressed as follows:

$$\chi^2 = \sum_{i=1}^N [\log(I_{cal}(\theta_i)) - \log(I_{exp}(\theta_i))]^2 \quad (9)$$

The reliability of the fitting was estimated by the R-value.

$$R(\%) = \sqrt{\frac{\chi^2}{\sum \log(I_{exp}(\theta_i))^2}} \times 100 \quad (10)$$

Before starting the least-squares calculation, approximate values for the thickness were estimated by Fourier transformation. At the initial stage of least-squares curve-fitting, the low angular region was used. Furthermore, the parameter δ was constrained to have the same values for the layers with the same material. The β parameters for different materials were fixed to the values, which are calculated from the bulk materials. Because β is usually 1 or 2 orders of magnitude smaller than δ , it has very little effect on the fitting results. Subsequently, the fitting region was increased, and the optimization calculation was repeated. By using this procedure, the fitting routinely converged in most cases.

2.4. Analysis by X-ray Photoelectron Spectroscopy (XPS), Auger Electron Spectroscopy (AES), Atomic Force Microscope (AFM)

In order to draw a density profile of thin films, it is necessary to determine the chemical composition of the film. To this end, the chemical composition was estimated from the X-ray photoelectron spectra, measured with an Escalab 2201-XL (VG) facility using monochromatized Al K α radiation. Fused quartz and sintered Si₃N₄, fractured in UHV

conditions, were utilized as reference materials in determining the chemical composition of SiO₂ and Si₃N₄ thin films [29]. Meanwhile, the layered structures of thin films and multilayers were also studied with Auger depth profiling using JAMP30. Also, surface morphologies of thin films were imaged with a NanoScope III atomic force microscope, operating in the tapping mode.

3. Examples of Characterization for Thin Films and Multilayer Films

3.1. Accurate Determination of Pt Film Density by XRR I 1 81

XRR has been used to determine density of thin films in the past. Wainfan et al. [30] have tried to measure the density of thin copper films by combining X-ray reflection measurement and chemical determination of the mass of copper films. Because of the limitation of their aligning precision, the errors of the density measurement were about 5%. In a recent paper, Schalchii et al. [31] presented the accuracy, as high as 0.7%, of density measurement with GIXR technique while they studied the dependence of density as a function of the thickness of silica thin films made by ultraviolet-induced chemical vapor deposition. Although the measurement accuracy has been listed and discussed in previous studies [30, 31], no result has been compared with other direct and reliable methods.

Mass measurement is one of the most reliable methods in determining density of uniform thin films, provided the thickness and the area of films are known. In the following, the accuracy and reliability of GIXR, comparing with the mass measurement results, are discussed. It should be mentioned that the system of Pt thin film on SiO₂ substrate is very suitable to measure the mass of the film with high accuracy, since metal Pt has a higher density and is stable in air.

In the experimental procedure, a 0.5-mm-thick ultrasmooth SiO₂ wafer was used for the substrate. Each SiO₂ wafer was cut into 4 pieces and Pt was deposited on to them in a molecular beam epitaxy (MBE) chamber. The SiO₂ substrates were weighed before and after the film deposition using a precisely calibrated microbalance with a sensitivity of 1 μ g (MT-5, Mettler). The weight of the samples was corrected by considering the floating force in air. The thickness of the films was determined by X-ray reflectivity analysis. The density of a film determined by gravimetry was calculated from its mass, thickness

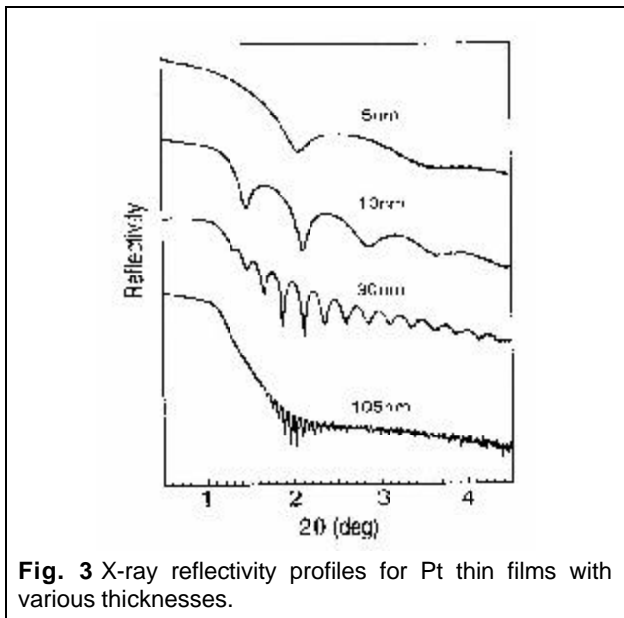


Fig. 3 X-ray reflectivity profiles for Pt thin films with various thicknesses.

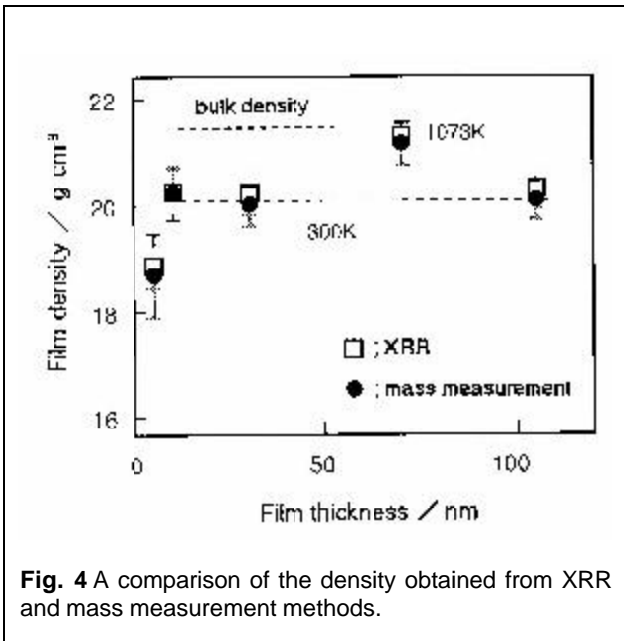


Fig. 4 A comparison of the density obtained from XRR and mass measurement methods.

and area values. X-ray reflectivity analysis independently gave the density of the film.

The Pt thin films, with thicknesses of 5, 10, 30 and 105nm, were prepared at room temperature. The X-ray reflectivity spectra of these Pt thin films are shown in Fig. 3. It can be found that there are significant differences in their XRR spectra. The oscillation frequency becomes lower as the thickness becomes thinner. In the 2θ range of 0.5 - 5.0° , only two oscillation peaks appear for the 5nm-thick Pt film. However, 10 strong oscillation peaks can be observed in the region between 1.6° and 2.4° for the Pt thin film

with a thickness of 105nm. The oscillation intensity becomes smaller and reaches the same level as the noise in the higher angle region.

Figure 4 compares the densities of Pt thin films obtained by the two methods. The error was defined as the double of a standard deviation. Every sample was measured five times. The results clearly show that both XRR and mass measurement methods give the identical density for the same sample within the error, 1.8%. The density of 105.27 nm Pt thin film is 20.30g/cm^3 , which is about 94% of the density of bulk Pt (21.45g/cm^3). The density of 73.98 nm Pt thin film grown at 1073K is 21.31g/cm^3 , which is close to the bulk one.

From Snell's law and noting that critical angle θ_c is usually very small, one can show

$$\delta = \theta_c^2 / 2 \quad (11)$$

Seen from equations (7) and (11), the density of XRR measurement is mainly determined by the critical angle θ_c . Therefore, instrument alignment is the most important limiting factor in precisely determining the density of thin films using the XRR method. A misalignment of 0.005° in sample tilt, with respect to the incoming X-ray beam, can change the final value of the electron density by 5% [32]. In our GIXR measurement, a very highly precise alignment as good as 0.0003° has been routinely achieved. This leads to very small experimental deviations. In fact, our results show that the GIXR experimental errors were about 0.37g/cm^3 in density (corresponding to 1.8%), 0.29nm in thickness (0.27%) and 0.05nm in surface roughness (2.3%) for the 105.27 nm Pt films.

3.2. Surface Roughness Measurement by XRR [19]

It is interesting to compare the surface and interface roughness determined by XRR and other techniques; for example, AFM. In the analysis of XRR profiles, the roughness is introduced in the exponential form of equation (3), supposing the roughness follows a Gaussian distribution, $\exp(-a\sigma^2)$. For a real interface, both interfacial roughness and diffuseness (shown in Fig. 5) have the effect of reducing the specular reflectivity of an interface either by scattering X-ray into non-specular directions, in the case of interface roughness, or increasing the transmissivity of the interface, in the case of interfacial diffuseness. In general, σ includes

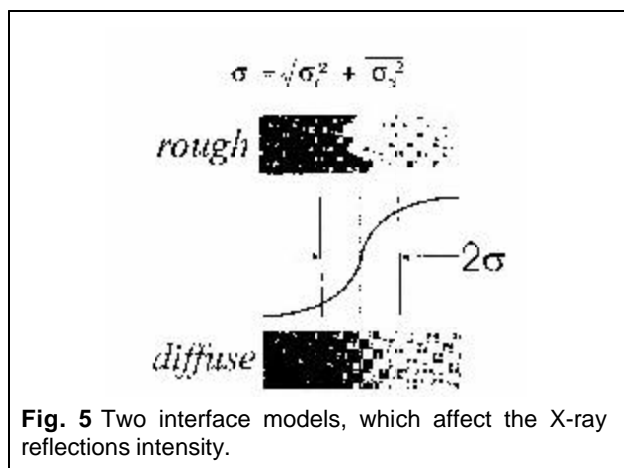


Fig. 5 Two interface models, which affect the X-ray reflections intensity.

interfacial roughness σ_r and interfacial diffuseness σ_d [33], i.e.

$$\sigma = \sqrt{\sigma_r^2 + \sigma_d^2} \quad (12)$$

Since XRR only records specular reflection intensity, and is only sensitive to the density difference along the normal surface direction, it cannot distinguish interface compositional grading or diffuseness from interface roughness. In this regard, grazing incidence diffuse X-ray scattering is an important complementary technique, which would separate interfacial roughness from interfacial grading [34]. If the specular reflectivity and non-specular diffuse scattering data can be fitted simultaneously with the same set of parameters, the XRR provides exact information on the interfacial roughness [35]. Otherwise, interfacial grading exists. To check the reliability of roughness measurement by XRR, a number of AFM measurements on surfaces of various thin films have been done (shown in Fig. 6). The results are summarized in Table 1. For the Pt film surfaces, the measured surface roughness by XRR is in good agreement with that by AFM. However, the roughness values measured by XRR are usually larger than those by AFM for other films. This is due to the surfaces of noble Pt thin films being very stable—the electron density around the surface regions does not change even if exposed to air. Therefore, the XRR measurements are consistent with the AFM results. On the other hand, the local electron density of the GaAs or SiO₂ surface, once exposed to air, would change due to oxidation or absorption of moisture. In this case, the measured roughness values by XRR would be larger than those by AFM measurements. In case of an oxide layer being formed; for example, Ta thin films [36]; it would be necessary to add a layer in

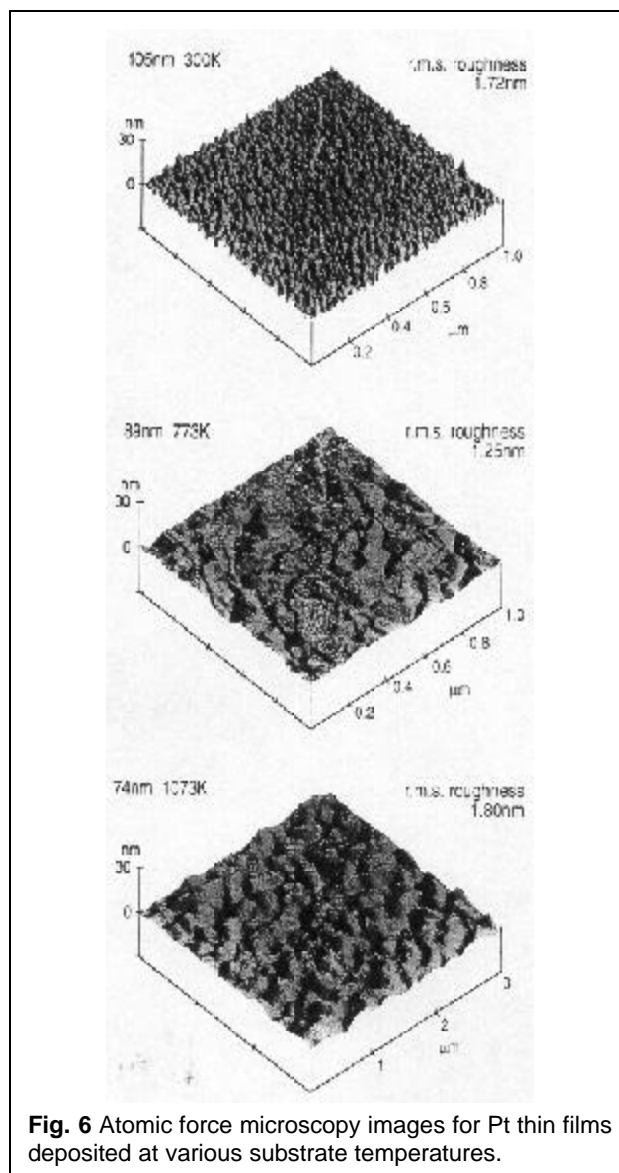


Fig. 6 Atomic force microscopy images for Pt thin films deposited at various substrate temperatures.

Table 1. Comparison in surface roughness between GIXR and AFM measurements

Thin films	Surface roughness (nm)	
	GIXR(σ)	AFM (rms roughness)
Pt(300 K) 105.3 nm	2.11±0.05	1.81±0.10
Pt(623K) 89.7 nm	1.59±0.03	1.50±0.10
Pt(773K) 89.5 nm	1.21±0.03	1.25±0.10
Pt(1073K) 74.0 nm	1.68±0.03	1.60±0.10
SiO ₂ /Si multilayer ^{a)}	0.65	0.33
Si ₃ N ₄ /Si multilayer ^{a)}	0.57	0.42
GaAs/AlAs superlattice ^{a)}	0.55	0.15

a) Refer to section 3.4.1 - 3.4.3

constructing the fitting model. However, it is not necessary, according to our experience, to assume a top oxide layer for Mo thin films [37].

3.3. Interfacial Structure between Sputter Deposited SiO₂ Film and Si(111) Substrate Surfaces [20-22]

Amorphous SiO₂ thin films are extensively used in the microelectronic industry as, for example, gate oxide, passivation and insulation of silicon and other elemental and compound semiconductor devices, or in higher density dynamic random access memory (DRAM) and larger flat panel displays. When the thickness is reduced to nanometer level, the interface would have a significant effect on their electric characteristics of thin films. Here, XRR was employed to characterize the SiO₂/Si interfacial structure.

Before deposition, the native oxide on the silicon surface was removed by dipping into diluted HF solution. In all the deposition runs, a SiO₂ target was used as the sputtering source, and argon was used as the working gas. In this case, there are three adjustable parameters which determine the structural properties of the deposited thin films; i.e. the rf sputtering power, the argon gas flow (or pressure) and the substrate temperature. The chemical composition was estimated by XPS measurement. The deposited films showed a chemical composition of 1 : 2 for Si : O, referring to the intensity ratio of Si 2p/O 1s for the fused silica surface fractured in UHV as the standard.

SiO₂ film was deposited by changing the substrate temperature from room temperature to 200, 350, 490, then 620°C. The deposition time was 60 min. for these films, except for the room temperature deposition where it was 30 min. Figure 7 shows the X-ray reflectivity for these samples. The dotted curves represent the experimental data and the solid curves stand for the fitted data. Obviously, the 200°C sample had the minimum amplitude and period of oscillations. On the contrary, the 620°C sample had the maximum amplitude and period of oscillations. This means that the samples had different thicknesses, while their deposition conditions were the same except for a different substrate temperature. In all cases, the total decay of the intensity was less than 6 orders within 3° (2θ), and the amplitude of the oscillations gradually increased with the increase of the reflection angle. To analyze the data, we first conducted a large number of simulations. If an abrupt transition from the a-SiO₂ thin film to c-Si occurs, a one-layer-model should work; and if there is a

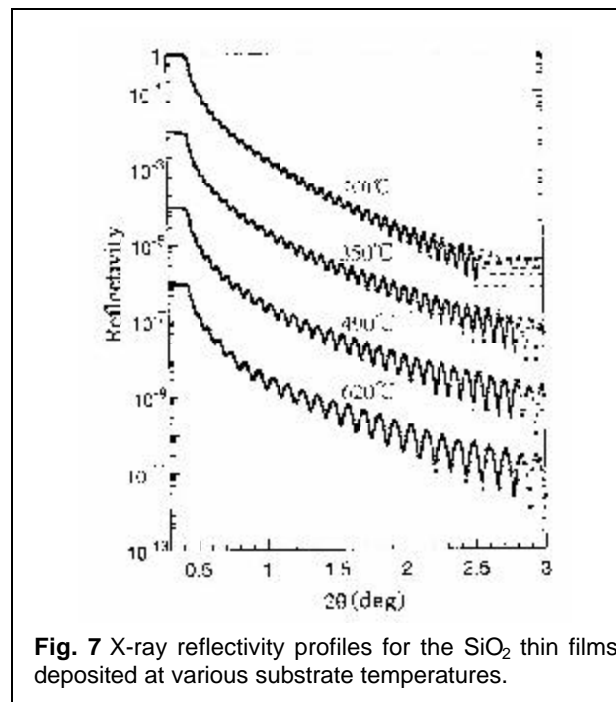


Fig. 7 X-ray reflectivity profiles for the SiO₂ thin films deposited at various substrate temperatures.

transition layer between the main SiO₂ layer and the Si substrate, a two-layer-model should be used. We checked the one-layer model, two-layer model, surface and interface roughness, density and layer thickness. We found that the one-layer model could not produce the observed oscillation features. Whether we changed the layer density or thickness, the oscillation amplitude of the simulated spectrum did not increase with the incident angle. It should be mentioned that surface roughness sometimes resulted in an increase in amplitude, but the characteristics were somewhat different. With the increase in surface roughness, the oscillation amplitude quickly increased and also decayed quickly, and the general intensity also decayed quickly (Fig. 8(a)). However, a thin higher density interface layer modulated the oscillation, but did not cause decay in general intensity. In the region between 0.3 and 3 degrees, the oscillation amplitude increased with an increase in the incident angle (Fig. 8(b)).

Based on the aforementioned knowledge from the simulations, we readily got the quantitative structural parameters of the samples by using a nonlinear least-squares curve-fitting technique. The results are summarized in Table 2. The deviations between measurement and calculation were very small. In all cases, the R-values were less than 1.2% for 200-490°C samples and about 2.4% for 620°C sample, which ensure the parameters such as the density, thickness, surface and interface roughness

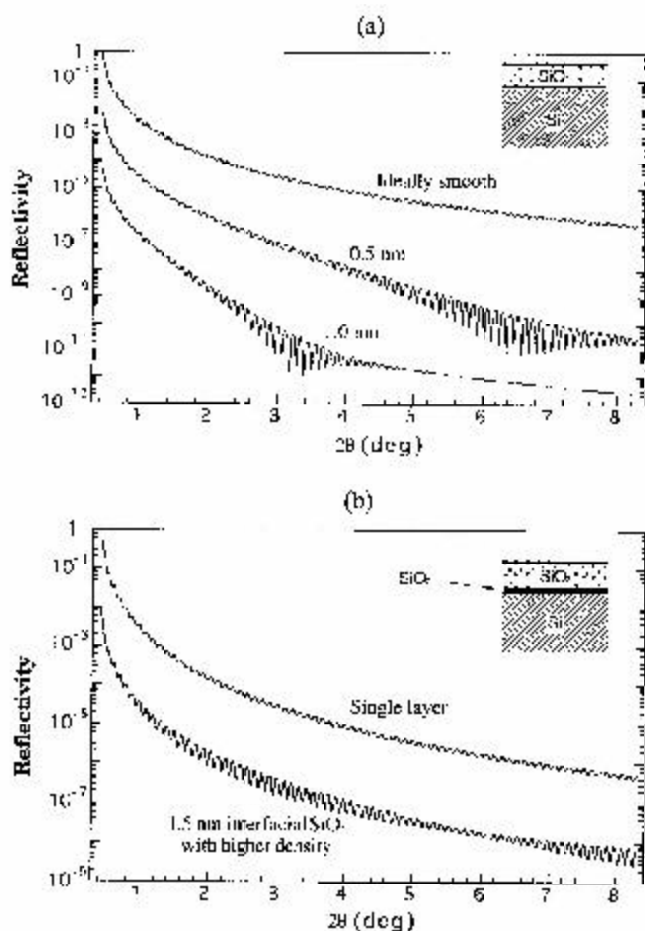


Fig. 8 The simulation results for an 80-nm thick SiO₂ film on a Si substrate: (a) effect of surface roughness on the X-ray reflectivity profile; (b) effect of a thin (1.5 nm) and higher-density (2.5 g/cm³) interface layer on the X-ray reflectivity profile.

Table 2 Structural parameters for group A samples ascertained from the XRR.

Sample	Layer	Density (g/cm ³)	Thickness (nm)	Roughness (nm)
RT	SiO ₂	2.19	65.80	0.80
	interface	2.05	0.70	0.57
200°C	SiO ₂	2.19	127.90	1.01
	interface	2.37	1.19	0.28
350°C	SiO ₂	2.19	114.62	0.76
	interface	2.52	1.32	0.36
490°C	SiO ₂	2.20	96.46	0.65
	interface	2.65	1.28	0.28
620°C	SiO ₂	2.20	76.24	0.57
	interface	2.67	1.61	0.23

reproducible and reliable. Here, a two-layer (an overlayer and an interface layer) model works very well. If a one-layer model is used, the XRR spectrum feature (the oscillation amplitude increases with the incidence angle) can not be reproduced. The calculated spectrum significantly deviates from the measurement data. Therefore, the R-value becomes very high and some parameters become abnormal. As can be seen in Table 2, the thickness of the thin interface layer between a crystalline Si and amorphous SiO₂ overlayer is about 1 nm, slightly increasing with temperature. As the substrate temperature was increased from 200 to 620°C, the density of the interface layer increased from 2.37 g/cm³ to 2.67 g/cm³. Qualitatively, this observation is supported by several other studies. Via a high-resolution core-level photoemission spectroscopy measurement, Grunthaner et al. [38] and Himpsel et al. [39] suggested a substoichiometric interfacial layer of compressed SiO₂ with

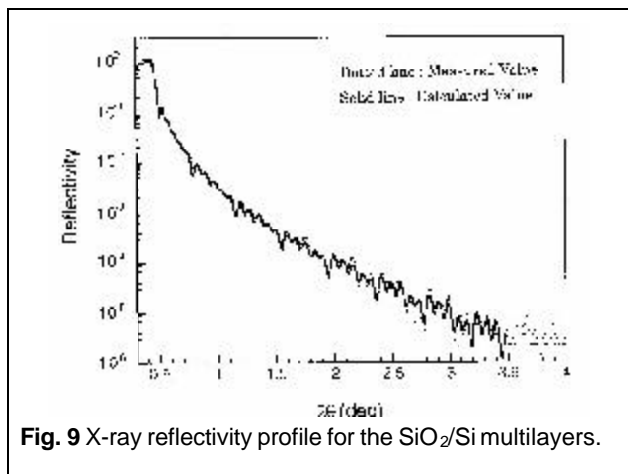


Fig. 9 X-ray reflectivity profile for the SiO₂/Si multilayers.

approximately 1 nm, and perhaps extending to 3 nm in thickness. Spectroscopic immersion ellipsometry [40, 41], which is an interface sensitive technique, detected a thin layer of higher refractive index, which was interpreted as a region of suboxide formation and compressed SiO₂. By using X-ray reflectivity, Awaji et al. [42] observed the presence of a higher-density (about 2.45 g/cm³) and thin (~1 nm) transition layer at the SiO₂/Si (100) interface. Rabedeau et al. [43] found that the electron density along the oxide/Si interfacial normal decays in an oscillatory manner from the Si surface, showing an ordered interface with a ~0.3 nm decay length. This finding is also in agreement with high resolution electron microscopy (HREM) [44] and grazing incidence X-ray scattering (GIXS) [45] studies of the SiO₂/Si interface. Both observed higher-density epitaxial microcrystalline phases SiO₂, such as tridymite or cristobalite.

Table 1 also shows that the total thickness of the silica films decreases from 129 nm to 78 nm, as the substrate temperature increases from 200 to 620°C. It indicates that the deposition may be influenced by the sticking coefficient of SiO₂ molecules on substrates. Increasing the substrate temperature will decrease the sticking coefficient, resulting in a lower deposition rate.

3.4. Characterization of Multilayers

3.4.1. SiO₂/Si multilayers [23, 24]

SiO₂/Si multilayers were prepared by rf magnetron sputtering for a surface analysis reference material. The nominal thickness of each layer is 20 nm. Figure 9 shows the X-ray reflectivity profile. The dotted line represents the experimental data and the solid line stands for the calculated data. It should be mentioned that here we set the following constraint

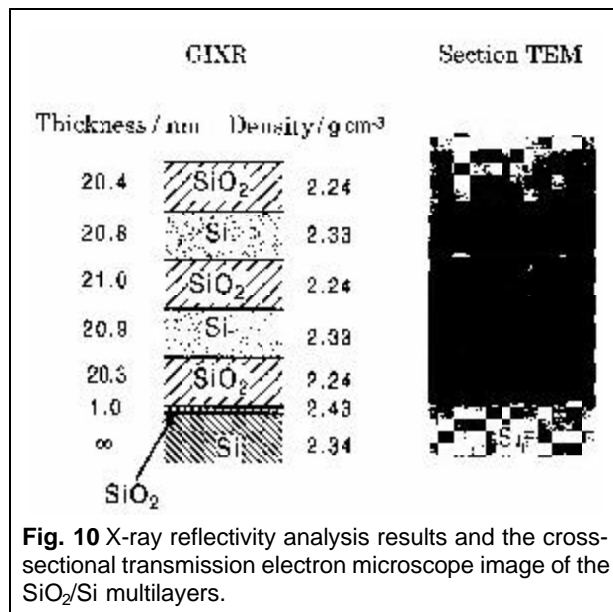


Fig. 10 X-ray reflectivity analysis results and the cross-sectional transmission electron microscope image of the SiO₂/Si multilayers.

conditions: all SiO₂ sublayers have the same δ and β , and so do the Si sublayers. However, the optical constants for the Si sublayer are not necessarily the same as those for the Si substrate since the Si film may have a density different from the Si substrate, due to the possible existence of microvoids or other defects in the films. To improve the fitting, and also based on knowledge from our previous study, we introduced an interface layer between the Si substrate and the first SiO₂ layer whose density was different from those of the SiO₂ and the Si layers. Following this modification, the R-value was 2.4%. The densities of SiO₂ layers are close to those of the thermal oxide films. The densities of the Si layers are close to that of the single crystal Si substrate.

TEM observation (shown in Fig. 10) confirms the XRR analysis. The difference in total thickness of the multilayers is within 2%, which is consistent with a previous study on SiO₂/Ta₂O₅ multilayers [15]. Although the density of the Si layers is close to that of the single crystal Si, there is no evidence of crystallization in the amorphous Si layers.

Figure 11 shows the Auger depth profile of the SiO₂/Si multilayers. The sputtering was carried out with 1 keV Ar ions. The experimental profile was recorded by plotting the peak-to-peak intensities of lock-in differential measurements for the Si LVV and the O KLL Auger signals. The depth resolution, calculated from the O KLL plots using 84-16% definition, changes, with increasing thickness, from 2.2 to 2.4 nm for the SiO₂/Si interface, and from 1.9 to 2.0 nm for the Si/SiO₂ interface. The depth resolution

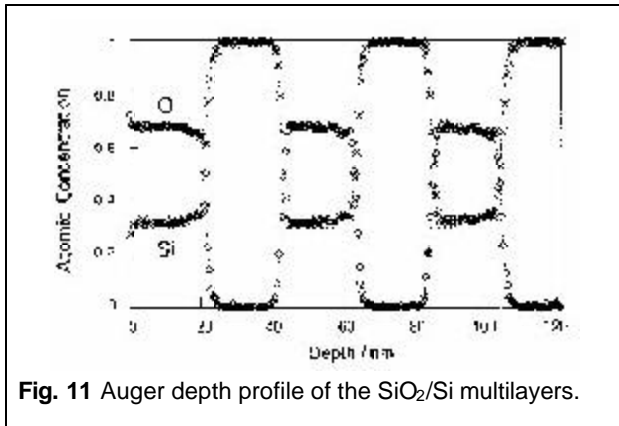


Fig. 11 Auger depth profile of the SiO₂/Si multilayers.

for the 5th interface is almost the same as that of the thermally oxidized film with the same thickness (100 nm). It is interesting that the depth resolution for the SiO₂/Si interface is slightly smaller than that for the Si/SiO₂ interface, which is contrary to the trend of the interfacial roughness change between the two kinds of interfaces. It is well known that the depth profile broadens at each interface since sputtering induces, for example, roughening and atomic mixing. However, the depth resolution does not significantly deteriorate with thickness, which suggests the advantages of our SiO₂/Si Multilayers for depth profiling applications.

3.4.2. GaAs/AlAs superlattices [25]

GaAs/AlAs superlattices with 4 periods were prepared on a n-type GaAs wafer by molecular beam epitaxy (MBE). Before the deposition, a 600 nm-thick GaAs buffer layer was deposited on the GaAs wafer. The substrate temperature during the deposition was kept at 600°C.

Figure 12 shows the X-ray reflectivity profile of the superlattices. The dotted line represents the experimental data and the solid line stands for the calculated data. An 8-layer model was applied for the fitting. After the final optimization, an R-value of about 3.1% was achieved. No constraint condition was employed for δ , thickness or roughness parameters during the final fitting. Table 1 shows the optimized values of parameters such as film density, thickness, and surface and interface roughness. For the density calculation, the chemical composition of GaAs and AlAs was assumed to be 1:1. The densities obtained were almost consistent with those of the bulk materials (5.32 g/cm³ for GaAs and 3.76 g/cm³ for AlAs). It is noted that the roughnesses of the GaAs layers are smaller than those of the AlAs layers. We often found such material-dependent systematic

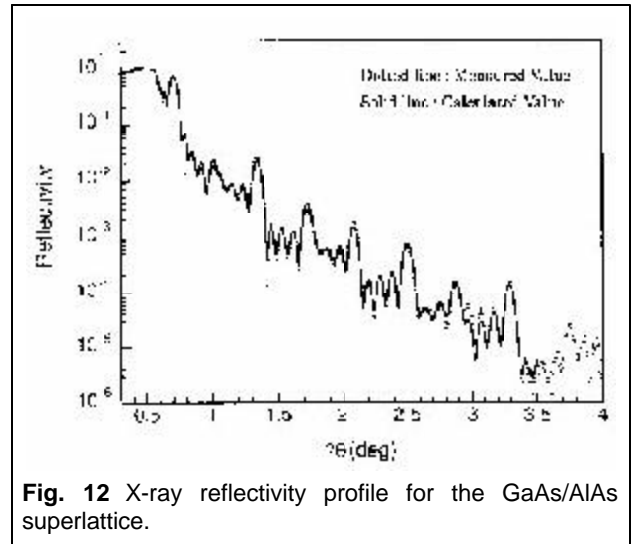


Fig. 12 X-ray reflectivity profile for the GaAs/AlAs superlattice.

roughness differences for multilayer films, such as the SiO₂/Ta₂O₅ Multilayers [15] and the other two multilayers described in this paper. This is probably related to the difference in surface free energy of different materials.

3.4.3. Si₃N₄/Si multilayers [25]

Si₃N₄/Si multilayer films were prepared by rf magnetron sputtering using a high purity Si target and a N₂ and Ar mixture gas as the sputtering gas. The chemical composition was controlled in a similar way to that described in our previous work [17].

Figure 13 shows the X-ray reflectivity profile for the Si₃N₄/Si multilayer films. The dotted line represents the experimental data and the solid line stands for the calculated data. The fit is very good when compared to the previous two samples, and the R-value converged at 1.7%. The δ values of all layers, as well as all the thickness and roughness parameters, were freed at the final fitting. The densities of the Si₃N₄ layers were about 3.0 g/cm³. Their density is smaller than that of the sintered material (3.44 g/cm³). However, it is closer to the densities obtained for amorphous thin films, between 2.8 and 3.1 g/cm³. The surface roughness of 0.57 nm was slightly larger than that of the interfacial layers. In addition, the interface roughnesses of the Si layers are a little smaller than those of the Si₃N₄ layers. A similar phenomenon was observed for the SiO₂/Si and Si₃N₄/Si multilayers. The higher roughness of the top layer compared to the interfaces is probably due to a reaction, like oxidation, which takes place on the surface after the film is exposed to air.

4. Conclusion Remarks

We have demonstrated the successful characterization of Pt thin films, SiO₂/Si interfacial structures, and GaAs/AlAs, SiO₂/Si, and Si₃N₄/Si multilayer by the XRR technique. XRR offers very high spatial resolution of sub-nanometer for the measurements of thickness, surface and interface roughness of thin films and multilayers. The high resolution and nondestructive features make it not only an important probe in exploring the structural nature of surface and interface scientifically, but also a promising tool in in-situ monitoring production processes of micro-electronic devices. Its high penetrating power makes it capable of probing surfaces under arbitrary conditions of pressure and temperature, and even solid-liquid interfaces, not limited to ultra high vacuum conditions like electron diffraction techniques. It should be mentioned that after the pioneering work by Parratt [27], XRR and the related scattering techniques did not develop immediately. Only the significant development of experimental techniques and instrumentation has made it possible in recent years. With the increase of the commercial X-ray systems for reflectometry and analysis of XRR spectra, XRR could become a popular technique for materials characterization, like X-ray diffraction, but not limited to crystalline structures, since GIXR works equally well for crystalline and amorphous thin films.

Acknowledgement

We would like to thank Drs. T. Fujimoto, K. Honda, N. Fukumoto for their cooperation in this research. Also, we would like to thank Prof. E. Horn of Rikkyo University for his valuable discussion.

References

- [1] "The National Technology Roadmap for Semiconductors Technology Needs" Semiconductor Industry Association, 1997 Edition.
- [2] H. Iwai and T. Momose, *Oyobutsuri*, **64**,1074 (1995).
- [3] G. C. Osbourn, *J. Vac. Sci. Technol.*, **B2**,176 (1984).
- [4] Y. H. Xie, D. Monroe, E. A. Fitzgerald, P. J. Silverman, F. A. Thiel, and G. P. Watson, *Appl. Phys. Lett.*, **63**, 2263(1993).
- [5] Y. H. Phang, D. E. Savage, R. Kariotis, and M. G. Lagailly, *J. Appl. Phys.*, **74**, 3181 (1993).
- [6] M. N. Baibich, J. M. Broto, A. Fert, F. Nguyen Van Dau, F. Petroff, P. Eitenne, G. Creuzet, A. Friederich, gentlemen. Chazelas, *Phys. Rev. Lett.*, **61**, 2472 (1988).
- [7] Japanese Standards Association, JSCA News, No. 4 (1996)
- [8] I. K. Kajiwarra and R. Shimizu, *J. Vac. Sci. Technol.*, **A13**, 1316 (1995).

Table 3 Structural parameters for the GaAs/AlAs multilayer film as determined by GIXR.

Layer	Density (g/cm ³)	Thickness (nm)	Roughness (nm)
GaAs	5.41	12.5	0.55
AlAs	3.69	9.5	0.90
GaAs	5.26	12.1	0.21
AlAs	3.67	9.6	0.80
GaAs	5.37	12.2	0.47
AlAs	3.78	9.6	0.74
GaAs	5.33	12.2	0.50
AlAs	3.74	10.0	0.55
Substrate	5.32	-	0.66

Table 4 Structural parameters for the Si₃N₄/Si multilayer film as determined by GIXR.

Layer	Density (g/cm ³)	Thickness (nm)	RMS Roughness (nm)
Si ₃ N ₄	3.02	22.4	0.57
Si	2.28	20.3	0.37
Si ₃ N ₄	2.95	21.7	0.39
Si	2.25	19.0	0.33
Si ₃ N ₄	2.98	20.1	0.41
Si(001)	-	-	0.40

- [9] ISO/REMCO N 471, March 1998.
- [10] E. Chason and T. M. Mayer, *Critical Rev. Solid State Mat. Sci.*, **22**, 1 (1997).
- [11] K. Stoev and K. Sakurai, *The Rigaku J.*, **14**, 22 (1997).
- [12] I. Kojima and H. Takaya, *J. Surf. Anal.*, **3**, 126 (1997).
- [13] I. Kojima, *Kogyo-zairyuu*, 47, 60 (1999).
- [14] I. Kojima, H. Takaya and E. Miyazaki, *Kagaku-kogyuu*, **50**, 22 (1999).
- [15] I. Kojima, B. Li, T. Fujimoto, K. J. Kim, and D. W. Moon, *J. Phys. D: Appl. Phys.*, **30**, 2143 (1997).
- [16] B. Li, H. Shen, Y. Saitoh, T. Fujimoto, and I. Kojima, *Thin Solid Films*, **315**,104(1998).
- [17] B. Li, T. Fujimoto, N. Fukumoto, K. Honda, and I. Kojima, *Thin Solid Films*, **334**,140 (1998).
- [18] I. Kojima, S. Wei, B. Li, and T. Fujimoto, *J. Surf. Anal.*, **4**, 70 (1998).
- [19] S. Wei, B. Li, T. Fujimoto, and I. Kojima, *Phys. Rev.*, **B58**, 3605 (1998).

- [20] B. Li, T. Fujimoto, and I. Kojima, *J. Vac. Sci. Technol.*, **A17**, 552 (1999).
- [21] I. Kojima, B. Li, and T. Fujimoto, *Surf. Interface Anal.* (in press).
- [22] B. Li, T. Fujimoto, and I. Kojima, *J. Phys. D: Appl. Phys.*, **32**, 1287 (1999).
- [23] N. Fukumoto, T. Fujimoto, B. Li, I. Kojima, and H. Takaya, *J. Surf. Anal.*, **4**, 414 (1998).
- [24] I. Kojima, N. Fukumoto, T. Fujimoto, B. Li, and H. Takaya, *J. Surf. Anal.*, **5**, 22 (1999).
- [25] I. Kojima, B. Li, and T. Fujimoto, *Thin Solid Films* (in press).
- [26] T. Fujimoto, B. Li, I. Kojima, S. Yokoyama, and S. Murakami, *Rev. Sci. Instruments* (in press).
- [27] L. G. Parratt, *Phys. Rev.*, **95**, 359 (1954).
- [28] S. K. Sinha, E. B. Sirota, and S. Garoff, *Phys. Rev.*, **B38**, 2297 (1988).
- [29] N. Fukumoto, B. Li, and I. Kojima, *J. Surf. Anal.*, **5**, 200 (1999).
- [30] N. Wainfan, N. J. Scott, and L. G. Parratt, *J. Appl. Phys.*, **30**, 1604 (1959).
- [31] A. Schalchii, J. J. Benattar, and C. Licoppe, *Europhys. Lett.*, **26**, 271 (1994).
- [32] W. E. Wallace and W. L. Wu, *Appl. Phys. Lett.*, **67**, 1203(1995).
- [33] D. L. Windt, *Computers in Phys.*, **12**, 360 (1998).
- [34] I. Papa, T. R. A. Hase, B. K. Tanner, and M. Wormington, *Physica*, **B253**, 278 (1998).
- [35] M. Chladek, V. Valvoda, C. Dorner, C. Holy, and J. Grim, *Appl. Phys. Lett.*, **69**, 1318 (1996).
- [36] K. Usami and H. Suzuki, *Nihon-oyo-jiki-gakkaishi*, **18**, 38 (1994)
- [37] Unpublished data.
- [38] P. J. Grunthaner, M. H. Hecht, F. J. Grunthaner, and N. M. Johnson, *J. Appl. Phys.*, **61**, 629 (1987).
- [39] F. J. Himpsel, F. R. Mcfeely, A. Taleb-Ibrahimi, J. A. Yarmoff, and G. Hollinger, *Phys. Rev.*, **B38**, 6084 (1988).
- [40] V. A. Yakovlev, Q. Liu, and E. A. Irene, *J. Vac. Sci. Technol.*, **A10**, 427 (1992).
- [41] Q. Liu, J. F. Wall, and E. A. Irene, *J. Vac. Sci. Technol.*, **A12**, 2625 (1994).
- [42] N. Awaji, Y. Sugita, S. Ohkubo, T. Nakanishi, K. Takasaki, and S. Komiya, *Jpn. J. Appl. Phys.*, **34**, L1013 (1995).
- [43] T. A. Rabedeau, I. M. Tidswell, P. S. Pershan, J. Bevk and B. S. Freer, *Appl. Phys. Lett.*, **59**, 706 (1991).
- [44] A. Ourmazd, D. W. Taylor, J. A. Rentshler, and J. Bevk, *Phys. Rev. Lett.*, **59**, 213 (1987).
- [45] R. H. Fuoss, L. J. Norton, S. Brennan, and A. Fischer-Colbrie, *Phys. Rev. Lett.*, **60**, 600 (1988).

